Delft University of Technology

Shearography non-destructive testing of thick GFRP laminates
Numerical and experimental study on defect detection with thermal loading

Tao, Nan; Anisimov, Andrei G.; Groves, Roger M.

DOI
10.1016/j.compstruct.2021.115008

Publication date
2022

Document Version
Final published version

Published in
Composite Structures

Citation (APA)
Tao, N., Anisimov, A. G., & Groves, R. M. (2022). Shearography non-destructive testing of thick GFRP laminates: Numerical and experimental study on defect detection with thermal loading. *Composite Structures*, *282*, Article 115008. https://doi.org/10.1016/j.compstruct.2021.115008

Composite Structures 282 (2022) 115008

Contents lists available at ScienceDirect

Composite Structures

journal homepage: www.elsevier.com/locate/compstruct

Shearography non-destructive testing of thick GFRP laminates: Numerical and experimental study on defect detection with thermal loading

Nan Tao [*], Andrei G. Anisimov, Roger M. Groves

Aerospace NDT Laboratory, Faculty of Aerospace Engineering, Delft University of Technology, Kluyverweg 1, 2629 HS Delft, the Netherlands

ARTICLE INFO

Keywords:
Thick composite
NDT
FEM
Digital shearography
Equivalent properties
Boundary conditions

ABSTRACT

Thick composite materials are commonly used as load-bearing structures in marine applications. Developing a suitable and sophisticated non-destructive testing (NDT) method for thick composites is an urgent challenge to improve the safety, reliability and maintenance of these structures. Digital shearography has become an important NDT technique for detecting defects in thin composite materials because of the advantages of high sensitivity to deformation change, and whole-field measurement. So far, the efficacy of shearography for thick composite inspection (e.g. thickness as more than 50 mm) has not been fully characterised. This paper combines finite element methods (FEM) and experimental tests to investigate the defect detection capabilities of shearography for inspecting thick glass fiber-reinforced polymer laminates. A thermal–mechanical model was established by computing equivalent thermal and mechanical properties and was evaluated by experimental shearography testing. In order to reliably simulate major defects in thick composite, flat bottom holes were manufactured in the specimen. Both simulations and experiments show that shearography is a promising technique to inspect thick composites. The thresholds for defect-induced phase change and the corresponding defect-induced deformation are determined for shearography testing of thick composites in this paper. Afterwards, the effect of mechanical boundary conditions on defect-induced deformation is studied by FEM.

1. Introduction

Fiber-reinforced composite materials [1–3] are used extensively in aerospace industry and marine applications because of their significant advantages in high specific stiffness and strength and load–carrying capability. However, with the existence of various kinds of defects such as delamination and fiber breakage, the material properties and structural integrity of composite materials may degrade severely [4]. Non-destructive testing (NDT) techniques are therefore needed to improve the safety and reliability of the structure. NDT of thin composite structures employed in aerospace engineering has been studied extensively for decades [5]; however, for NDT of thick composite structures (e.g. 10–50 mm thick), which are normally used as load-bearing structures in marine applications, little attention has been paid. So far, the NDT defect detection capabilities and inspection limitations for thick composite have not been fully characterised.

Ultrasonic testing is one of the most well-known NDT methods [1]. It uses high frequency acoustic waves to detect composite structural anomalies such as cracks or delaminations [3,7]. During the last decades, advanced ultrasonic testing methods including phased array ultrasound testing [3], air-coupled ultrasonics [8], and laser induced ultrasound [1] have been developed for defect detection. Although it has been widely used in industrial inspection for a long time, the attenuation, scattering and multiple reflections of ultrasound signals can become a significant issue when inspecting thick composites. Besides, it can be quite time-consuming to scan the whole structure. Therefore it is a challenge to apply it for inspecting thick composites. Vibration analysis [9–13] and X-ray radiography [5,7] are also well-known NDT methods for inspection of composite materials. They have their own disadvantages and limitations when inspecting thick composites. For vibration analysis, which reveals the presence of defects by detecting changes in dynamic properties (e.g. stiffness, natural frequency) of the composites, it may suffer from a significant signal loss for inspecting deeply buried defects [5,7]. For X-ray radiography, one of the major challenges is its inability to detecting defects in the through-thickness direction, and the danger associated with X-ray to humans can be a problem as well [5,7]. Among the various NDT methods in the existing literature, Shearography [6,14–20] is an optical interferometric

---

[*] Corresponding author.
E-mail address: n.tao@tudelft.nl (N. Tao).

https://doi.org/10.1016/j.compstruct.2021.115008
Received 7 June 2021; Received in revised form 2 November 2021; Accepted 15 November 2021

technique with the advantages of high-sensitivity to deformation change, full field, robustness to environmental disturbances, real-time results, and non-contact measurement. It directly measures derivatives of surface deformation, which are closely related to surface strain components. This allows shearography to inspect structures by looking for defect-induced anomalies in the surface strain field, from the fringe pattern and/or phase map. A vital procedure for shearography NDT is to load the tested object during inspection. The loading techniques used in shearography for defect detection [1,16,21] include thermal, vacuum, pressure, vibration, microwaves, and so on. Since shearography can detect surface displacement gradient changes in the range of micro-strain, the applied stress does not have to be very large (e.g. heating by several degrees centigrade).

It should be noted that the key to a successful shearographic inspection lies in highlighting the contribution of defect-induced deformation (DID, representing defect signal) in the overall deformation (OD, representing background signal). Defect detection is expected to succeed as long as the defect signal is large enough for shearography to detect (e.g. the ratio of defect signal to background signal is greater than two). Moreover, it is possible to remove or reduce the background signal for detailed inspection by subtracting a fitting surface that indicates overall deformation. So far, in shearography NDT of thick composites, the defect-induced response in shearograms to loading methods (e.g. mechanical, thermal, or impact loading) and loading parameters (e.g. loading time or loading intensity) is not fully understood yet. In literature, studies on combining finite element method (FEM) with digital shearography have already been reported for improving the interpretation of shearograms [22–24]. Akbari et al. [25] studied the thermal loading parameters in a shearography test by using a numerical-experimental approach. More recently, Yang et al. [26] simulated defect detection of thin materials under various loading scenarios, by evaluating the ability of detection with shearography. Buchta et al. [27] combined finite element analysis with shearography testing to monitor artwork. The above-mentioned studies were focused on thin metal plates or thin composite materials (less than 6 mm in thickness). The applications were either for qualitative inspections [16] or the number of major defects studied in literature was limited (1–2 artificial defects) [24,25,27]. Though applications for shearography NDT of thin composite materials were well discussed in literature, but the experimental research for thick composite inspection with shearography was conducted by few researchers [28,29]. To the best of our knowledge, no literature has reported on a numerical-experimental study on the defect detection capability of shearography in thick fiber reinforced composite laminates (with the thickness of more than 50 mm), which is the main objective of this investigation. Besides, the investigation of DID to different loading conditions such as loading time and loading intensity for shearography NDT of thick composites has not been reported. Moreover, there is little research about the effect of boundary conditions on DID of thick composite. Shearography NDT of thick composite is challenging considering the complexity in material structures, the significant thickness and the high stiffness of the thick composites [5,7,30]. We aim at broadening of this shearography application to composites with thickness as up to 50–60 mm that are common in marine sector.

This paper aims to investigate the defect detection capabilities of shearography in thick composites subjected to thermal loading. For that, a thermal–mechanical model has been built in ABAQUS to assist in the shearography inspection. To reliably simulate major defects in thick composites [23,25], flat bottom holes were made following a standard practice to represent a single delamination. The specimen description and shearography theory are introduced in Section 2. Section 3 details the thermal–mechanical model of the thick glass fiber reinforced polymer (GFRP) laminate. Equivalent mechanical and thermal properties are calculated for modelling. This section also presents a method to characterize the heat flux of heating lamps. In section 4, the comparison of FEM and experimental results are conducted for both transient temperature and surface strain. Based on the confined FEM models and shearograpy results, the defect responses of the thick composite during cooling are studied. Afterwards, the effect of mechanical boundary conditions on defect deformation of the thick composite are analyzed by FEM.

2. Specimen and shearography theory

2.1. Specimen description and material properties

E-glass based composites have found widespread applications in marine area due to the advantages of lightweight construction, corrosion resistance and cost-effectiveness [31,32]. However, various defects (e.g. delaminations, fiber breakage, water ingress) [1] may occur within those composites under a harsh and aggressive marine environment. For the purposes of the current study, an E–glass/vinylester panel representative of a marine composite, with a total thickness of 51 mm was manufactured by Damen Shipyards. A schematic of the panel is shown in Fig. 1. This GFRP panel is a representative test specimen for composite ship construction. The stacking sequence of the specimen is $[0/+45/90/-45]_{60}$ with the size of 600 × 450 mm^2. The specimen was milled with 13 flat bottom holes with three different diameters (D = 30, 60, 120 mm). These defects are at different depths (Z) ranging from 5 to 40 mm, and represent major defects of thick composites. Here the selection of layup, thickness of the material, defect depth and size are representative for marine composites. It should be noted that the depth of an artificial defect is defined in this paper as the remaining thickness of the material after drilling. Each artificial defect has been named by an alphanumerical code. For example, “D60–Z15” represents the defect that is 60 mm in diameter and at 15 mm depth. In this study, we used one specimen as shown in Fig. 1 for characterising the defect detection capabilities of shearography NDT for thick composites.

Table 1 shows the experimentally measured material properties of the specimen. For that, 87 small samples (4 layers of fiber) were designed and manufactured to measure the Young’s modulus, shear modulus and poisons ratio in different directions according to ASTM Standards D3039/D3039M-14 [33], D3410/D410M-03 [34], and D7078/D7078M-12 [35], respectively. 15 tests were performed for determining each one of the in-plane material properties and 6 tests were performed for determining each one of the out-of-plane shear properties. The tensile tests were performed by using the Electromechanic Universal Test Machine, and the compressive tests were was performed by using a using a Zwick Materials Testing Machine. A Material Test 810 System was used for the shear tests. Besides, the density and the fiber volume ratio were determined by using a Mettler Toledo (AB204-S) balance and a Nabertherm oven (30–3000 °C), respectively. The thermal expansion coefficients of the laminate were measured with thermomechanical analysis (TMA) on a Perkin Elmer Diamond TMA, and the specific heat of the laminate was measured with modulated differential scanning calorimetry (MDSC) on a Perkin Elmer DSC 8000.

It should be noted that the out-of-plane elastic modulus, the out-of-plane Poisson’s ratios, and the thermal conductivities of the ply are unknown. For a single ply, it was assumed that $E_{33} = E_{22}$ and $\nu_{13} = \nu_{12}$. Out-of-plane Poisson’s ratio ν_{23} was calculated based on the self-consistent field model [36]. In order to calculate thermal conductivities in Table 1, we first obtained the material properties of the resin and glass-fiber from the material manufacturer and previous projects [37]. Then the micro-mechanical relations (the Halpin-Tsai equations) were applied to calculate thermal conductivities along and transverse to the fiber directions [38].

2.2. Digital shearography

A schematic diagram of a representative shearography system based on a Michelson interferometer is shown in Fig. 2. This shearograhy setup is adapted to measure the out-of-plane surface displacement gradient as delaminations and flat bottom holes are expected to affect the out-of-

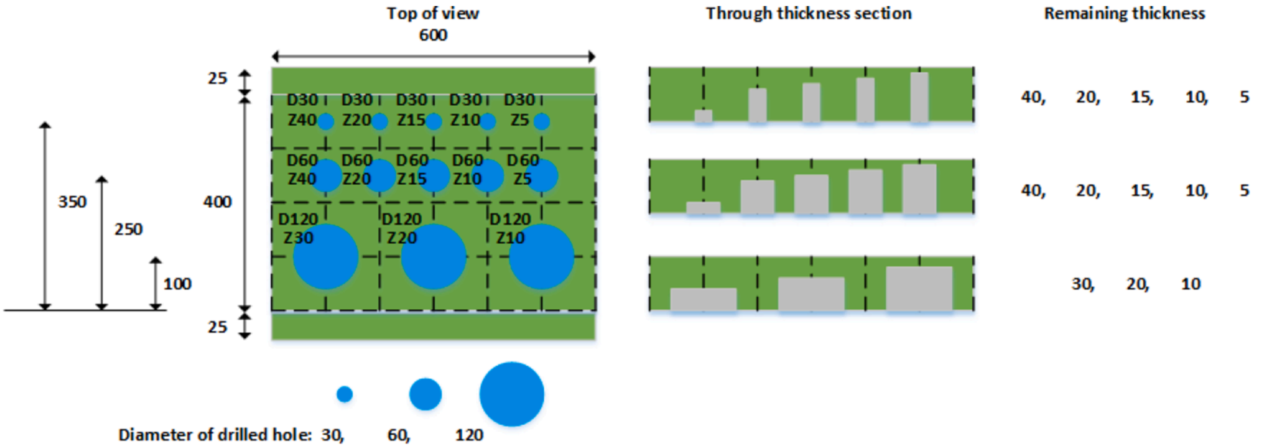

Fig. 1. Diagram of the specimen with flat bottom holes. All dimentions are in mm.

Table 1
Material properties for E-glass fiber/vinyl ester resin laminate.

Property	Unit	Value	Description	Reference
E_{11}	GPa	37.9	Elastic modulus of a ply	[33]
E_{22}	GPa	12.0		[33]
E_{33}	GPa	12.0		$E_{33} = E_{22}$ assumed
G_{12}	GPa	5.0	Shear modulus of a ply	[35]
G_{23}	GPa	4.1		[35]
G_{13}	GPa	3.7		[35]
ν_{12}	$[-]$	0.3	Poisson's ratios of a ply	[33]
ν_{13}	$[-]$	0.3		$\nu_{13} = \nu_{12}$ assumed
ν_{23}	$[-]$	0.4		[36]
α_x	$10^{-6}/^{\circ}C$	19.18	Coefficients of thermal expansion of the laminate	TMA
α_y	$10^{-6}/^{\circ}C$	20.81		TMA
α_z	$10^{-6}/^{\circ}C$	46.80		TMA
c_p	j/(kg°C)	803	Specific heat at 20 °C	MDSC
ρ	kg/m^3	1971	Density	Mettler Toledo
Vf	[%]	57	Fiber volume ratio	Nabertherm
k_1	W/m°C	0.81	Thermal conductivity along fiber direction	[38]
k_2	W/m°C	0.36	Thermal conductivity transverse to fiber direction	[38]
k_3	W/m°C	0.36	Thermal conductivity through thickness direction	[38]

plane deformation. By using a beam expander, a laser beam is expanded to illuminate a rough surface, creating a speckle pattern [Fig. 2(a)]. Two images (identical but sheared) are generated by tilting the shearing mirror by a small angle, [Fig. 2(b)]. In this way, the scattered light from two neighbouring positions on the rough surface of the object can be brought to meet in the image plane of a CCD camera, interfering with each other to form an interferometric speckle image. In this work the shearing device is able to control the direction and the amount of the shearing δx [Fig. 2(b)].

The recorded intensity of the speckle pattern by camera can be written by [15,39]:

$$I = I_0(1 + \gamma cos\phi) \quad (1)$$

where I_0 represents the background intensity, γ represents a term that indicates the fringe modulation, and ϕ represents a random relative phase between the two neighbouring points, separated by δx.

Defect detection by shearography relies on comparing two deformation states of the object. Two sets of images (reference images and signal images in Fig. 2(c)) are captured during measurement. The reference images can be captured either before or after loading, and the signal images are usually captured after loading. Computing the difference of the phases between the two states of deformation yields the phase difference ($\delta\phi$), which is also known as fringe pattern:

$$\delta\phi = \phi^{'} - \phi \quad (2)$$

it can be noted that $\delta\phi$ represents the optical phase difference introduced by loading, which is proportional to the displacement gradient in the shearing direction.

By making the observing and illuminating directions normal to the object surface, if the shearing amount (δx) is small enough and the shearing direction is parallel to the x-axis, the optical phase difference can be approximately represented by a strain component or out-of-plane displacement derivative:

$$\delta\phi_x = \frac{4\pi}{\lambda}\frac{\partial w}{\partial x}\delta x \quad (3)$$

Eq. (3) shows that when considering an image rather than a single point, shearography can detect flaws by finding strain anomalies from out-of-plane surface strain field. When the shearing direction is along the y-axis, the surface strain components in y direction ($\partial w/\partial y$) can be obtained by replacing x with y in Eq. (3).

As mentioned before, as shearography reveals a defect in an object by comparing the speckle patterns between two states of deformation, some form of loading or stressing is required to be applied to the object being inspected. This research is focused on thermal loading because of its interest for industrial applications.

3. Numerical modelling

Note that as the composite laminate ($[0/+45/90/-45]_{60}$) studied in this paper consists of large numbers of a repeating sublaminate, effective mechanical and thermal properties have been calculated for the laminate for use in the modelling in order to save memory and computational time.

3.1. *Effective mechanical and thermal properties for thick composite modelling*

In literature, several mathematical methods have been reported to determine the equivalent elastic properties of laminates [40–44]. Among them, Sun and Li [43] derived expressions of effective elastic constants for thick laminates by employing a longwave concept. Hoorn

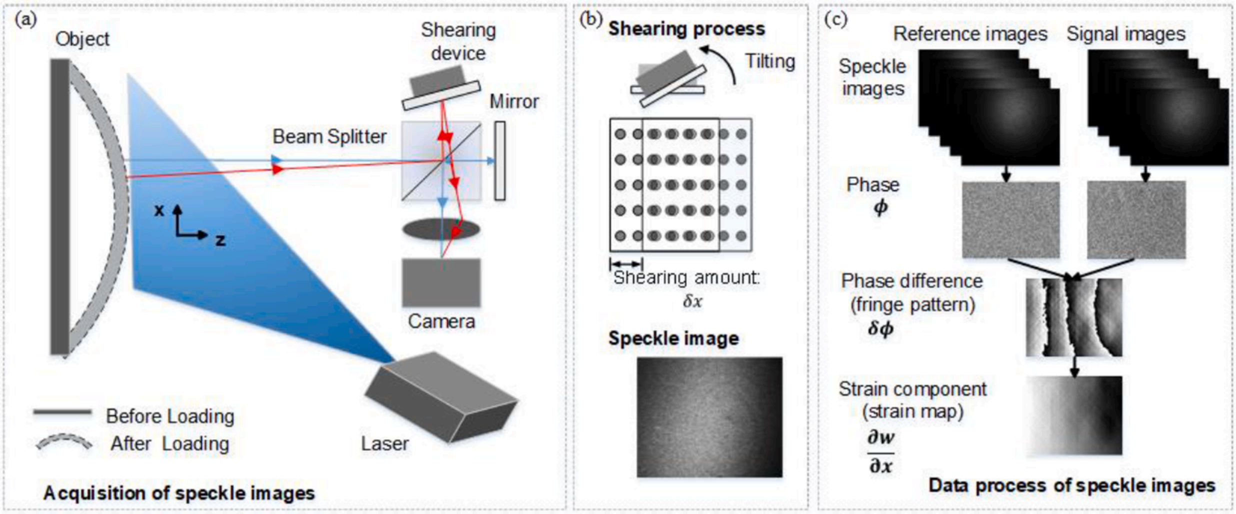

Fig. 2. Diagram of shearography system for the out-of-plane displacement gradient (shearing along *x*-direction).

et al [44] derived expressions for equivalent laminate mechanical properties with the equal strain assumption. Both of the methods can obtain three-dimensional elastic properties and the results from the methods derived in [43] and [44] are compared in this paper.

As shown in Table 2, the equivalent elastic modulus for composite laminate with substructure [0/45/90/−45] are computed according to [43] and [44], respectively. Results calculated from the two methods agree with each other well. Since the differences between the equivalent mechanical properties derived from the two methods are small (less than 1%), either method is feasible. In this study, the method in Ref. [44] was used for further modelling due to its ease of application.

Equivalent thermal conductivities of the laminate are also needed for modelling. The expressions derived in [45] are applied to determine the global conductivities of three directions for the thick laminate. For the GFRP laminate used in this research, the effective thermal conductivities k_x, k_y, k_z (W/m•°C) in the x, y, and z directions are 0.585, 0.585, and 0.36, respectively. Since the equivalent properties of the thick composite laminate can be derived, the laminate was modelled by using its equivalent properties.

3.2. Thermal-mechanical model

Fig. 3 shows the thermal–mechanical model developed in ABAQUS to simulate the thermal deformation of a thick composite laminate with flat bottom holes. The specimen is freestanding on an optical table during measurement. To simulate this mechanical boundary condition in Abaqus, the displacement of the bottom surface along y-direction is constrained (UY = 0 for bottom surface). To compensate heat loss from the composite to environment, a heat transfer coefficient needs to be applied to the model. In literauture, the free convection heat transfer coefficient of gas [46] is 2–25 W/m^2·K, and considering that the air flow in the lab is relatively small, therefore we selected a small value (5 W/m^2·K) for the model as a thermal boundary condition. The eight-node coupled temperature-displacement element (C3D8T) was selected for the finite element analysis since it is a 3D element and has thermo-mechanical capabilities. This C3D8T element measures displacements (e.g. displacements in x, y, z-axis, U1, U2, U3), strains (e.g. E11, E22), as well as temperature of the whole model. In areas with defects, the mesh is refined (2 × 2 mm^2 in size) in order to get a more accurate result for the defect response, while in healthy regions, the mesh density decreases (5 × 5 mm^2 in size) to reduce computational time. The element number through thickness direction is 60 (one element per equivalent layer). This created a finite element model consisting of about 700,000 elements and the total computational time was about 30 h using a high performance computing cluster. In this research, the thermal deformation of the whole specimen during 180 s heating and 320 s cooling is simulated to assist in the shearography NDT. The selection of the heating and cooling times is based on the efficacy of defect detection of D60-Z15, which is the main defect size of interest for this study. These values were empirically obtained from experiments.

Table 2
Comparison of effective modulus predictions for GFRP laminates.

		[0/45/90/−45]		Difference	
	Unit	Ref. [43]	Ref. [44]	Absolute	Relative
E_x	*GPa*	20.667	20.703	0.036	0.17%
E_y	*GPa*	20.667	20.703	0.036	0.17%
E_z	*GPa*	13.275	13.275	0	0
G_{xy}	*GPa*	8.094	8.117	0.023	0.28%
G_{yz}	*GPa*	3.897	3.909	0.012	0.30%
G_{xz}	*GPa*	3.897	3.909	0.012	0.30%
ν_{xy}	[−]	0.277	0.275	0.002	0.72%
ν_{yz}	[−]	0.309	0.309	0	0
ν_{xz}	[−]	0.309	0.309	0	0

The specimen was heated from the front by two halogen lamps. Here the front side represents the specimen surface where the flat bottom holes are not visible. To simulate transient temperature and thermal deformation during inspection in Abaqus, surface heat flux is needed as an input of thermal loading. Due to limited direct measurement options, an indirect reconstruction of the surface heat flux was perfomed by solving an inverse problem from the thermal response (transient temperature) which was measured by a surface mounted thermocouple (TC). Further in the model, an assumption of a uniform heat distribution is made. Considering the specimen is relatively thick (51 mm) and the thermal conductivity is relatively small, the surface temperature on the heating side for the first couple of minutes during heating can be represented by the analytical solution of the semi-infinite solid with constant surface heat flux [46]:

$$T(t) = T_i + 2q_0\left(\frac{t}{\pi\rho c_p k_z}\right)^{\frac{1}{2}} \tag{4}$$

where T_i is the initial temperature of the plate (20 °C, representing room temperature in the lab), q_0 is the heat flux at the front surface by the halogen lamps, and t is time during heating. Since the transient temperature in time can be measured with the TC, and the material prop-

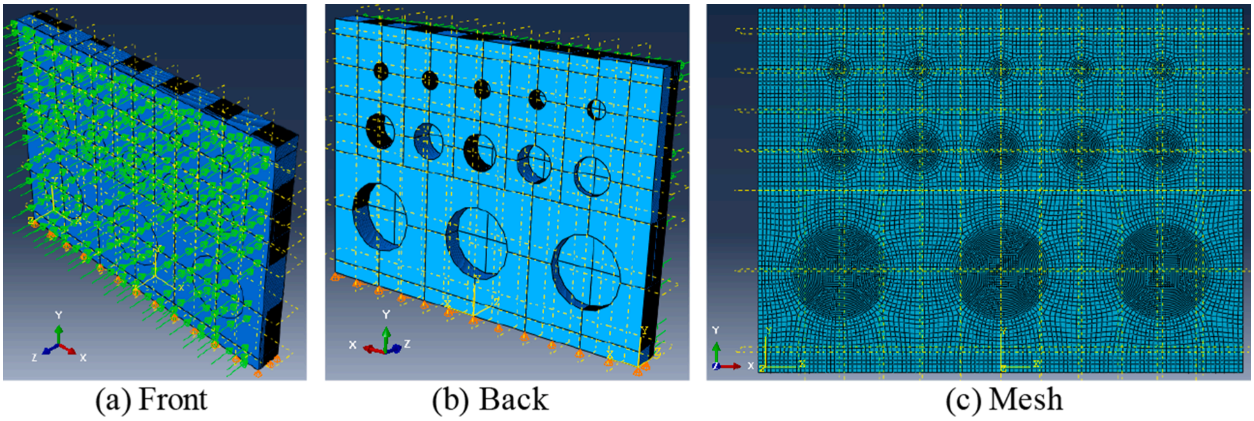

Fig. 3. The 3D FEM model developed in Abaqus.

erties including density ρ, the specific heat c_p, and the thermal conductivity through thickness direction k_z are already known, so the only unknown parameter is the heat flux q_0, which is assumed to be a constant due to the assumption of the uniform heat. The characterization of the unknown value of heat flux q_0 is solved through a curve-fitting process. The transient temperature at the front surface of the central hole (D60-Z15) during heating is shown in Fig. 4(a). The estimated heat flux is 285 W/m^2. As shown in Fig. 4(b), at the beginning of the heating, the maximum difference in temperature between the experimental result and the analytical solution is around 0.4 °C. The difference narrows down to 0.1 °C as the heating time increases from 30 s to 180 s, indicating that the estimated heat flux matches experimental data well.

It should be noted that in the real experiment, the thermal condition of uniform heating is satisfied approximately for the region near D60-Z15, while for the region far from D60-Z15 (e.g. the edge of the specimen), the real surface heat flux may differ a bit from the estimated heat flux 285 W/m^2. Therefore, it is expected that the difference between experiments and simulations can increase as from region near central hole to region close to the edge. For this study, the uniform heating condition is acceptable since the field of view (FOV) for shearography NDT is about 3/10 of the whole specimen, so the edge area is outside of the FOV, and from the perspective of validation of modelling, we can first focus more on the region near D60-Z15, which is done in the following section.

4. Results and discussions

As described in Section 3.2, a full-scale, thermal–mechanical model for thick composite was established to predict the specimen’s deformation during heating and cooling. In this section, first the FEM model was evaluated by comparing numerical results to experimental ones for transient temperature and surface strain components ($\partial w/\partial x$). The transient temperature was measured by TCs at the front (defect-free side) and rear surfaces of the specimen and the surface strain component was measured by shearography from the front. Then the DID during cooling was investigated by shearography and FEM. Afterwards, the influence of the mechanical boundary conditions on the DID detectability was analyzed by FEM.

4.1. Comparison between FEM and experiments

Fig. 5 (a) shows the positions of four TCs which were glued to the specimen. Two of them were attached to points A1 and A2, measuring temperature of the front and rear surfaces of D60-Z15, the other two were attached to points A3 and A4, measuring temperature of the front and rear surfaces of intact part. Although more TCs could give more information on the distribution of the temperature and heat flux, however, more TCs may also affect the measurement of shearography. Therefore, the number of TCs is minimized to not interfere with shearography measurement. Fig. 5(b) shows the measurement area for the shearography tests. As a result of working conditions and instruments, a measurement of the full area of the specimen was not feasible. The FOV of the camera is about 320 × 280 mm^2 of the specimen. It is reported [47,48] that in shearography steup, the shearing amount across the whole FOV may be not the same due to aberrations and wave front errors of the optical elements. In this paper, a calibration process [48] for the shear amount δx over 250 × 185 mm^2 of the FOV was implemented to reduce errors resulted from the shear variation across the specimen surface. As mentioned in Section 2.2, the reference interferograms for shearograhy can be captured either before or after loading, so the influence of the reference status for defect detection by shearography was also studied here.

Fig. 6(a) shows a comparison of transient temperature between experiments and simulations at points A1 and A2, respectively. The lamps

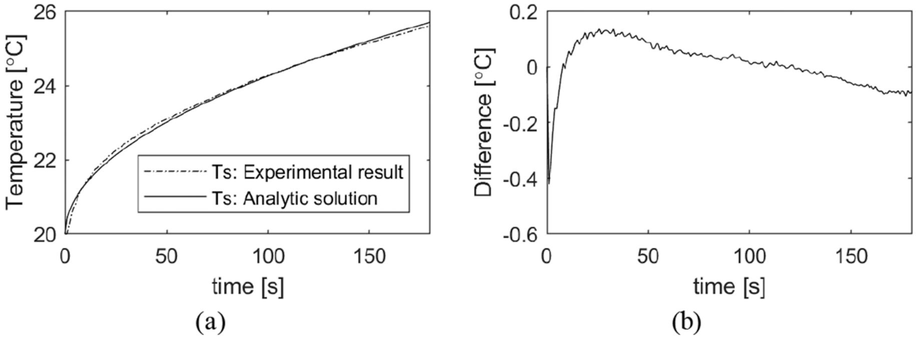

Fig. 4. (a) Transient temperature measured with a TC and predicted by theory at the front surface of the central hole (D60-Z15). (b) Temperature difference between the experimental result and the analytical solution.

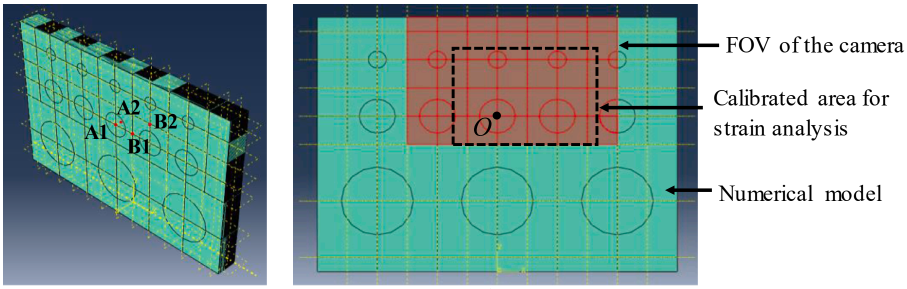

(a) (b)

Fig. 5. (a) Positions of TCs. (b) The measurement area for shearography tests.

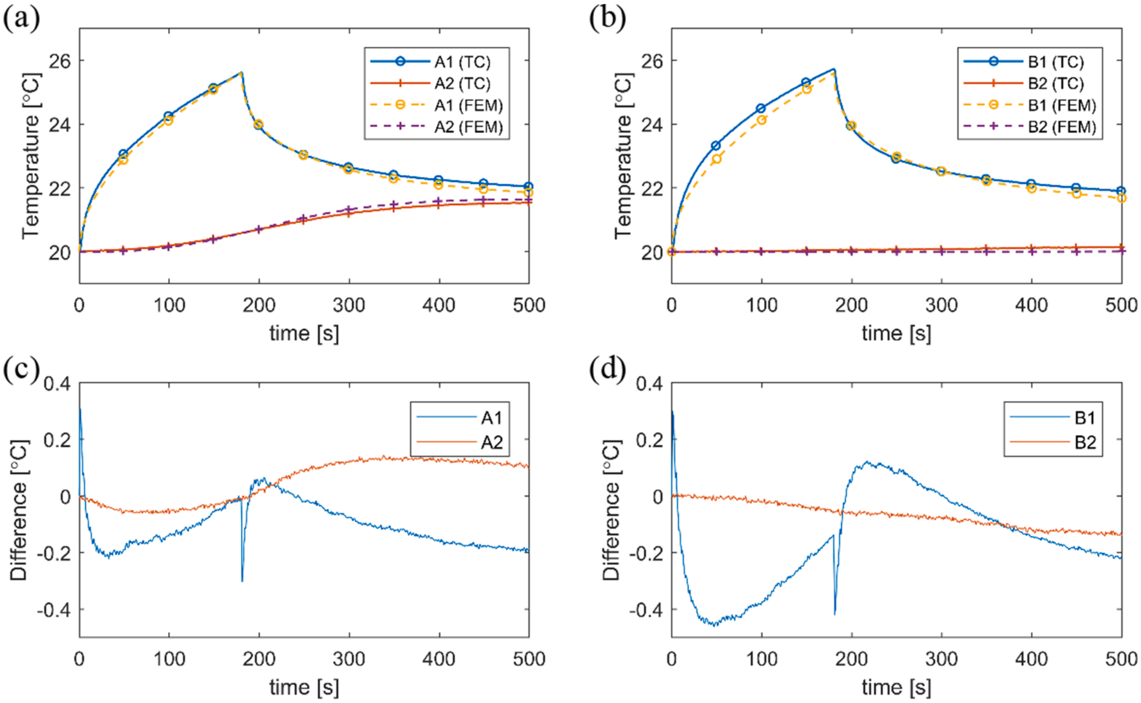

Fig. 6. Comparison of transient temperature between experiments and simulations. (a) At the central hole (D60-Z15). (b) On a healthy part. (c) - (d): Differences in temperature between experiments and simulations at A1, A2, B1, B2, respectively.

were on from time 0 to 180 s and off from time 180 to 500 s. After turning the lamps off, the temperature of the front side decreased immediately while the temperature of the rear side still increased during cooling. Similar phenomenon can be found in Fig. 6(b). The temperature increment at B2 (~0.1 °C) is much lower than that at A2 (~1.5 °C), since the thermal conductivity is relatively small and the thickness of the intact part (51 mm) is much larger than that of the central hole (15 mm), so it takes much more time for heat to reach B2. The transient temperatures between experimental measurements and FEM results agree with each other well. The differences in temperature between simulations and experiments at four positions are shown in Fig. 6(c) and (d). A disturbance in temperature difference occurs in Fig. 6(c) and (d) in the initial stage of cooling. This is because in the experiment, it takes 2 s for the lamps to turn off completely. In this 2–second transition period, the heat flux from the lamps decreases rapidly to 0, while in the modelling, the heat flux is assumed to be zero right after heating, so a short pulse-like disturbance was induced in temperature difference.

Fig. 7 shows strain maps at t = 180 s (right after heating) and t = 500 s (cooling for 320 s), respectively. The reference speckle images were captured before heating. The representative out-of-plane displacement derivative maps at 180 s and 500 s derived from FEM and shearography, and their corresponding differences are given in Fig. 7(a)–(c) and (d)–(f), respectively. Since the primary outputs from Abaqus software are displacements rather than displacement derivatives, a MATLAB code was developed to calculate the displacement derivative data from the Abaqus output. As mentioned before, the modelling is a full-scale simulation while the calibrated area for shearography is 250 × 185 mm^2 of the simulated object, therefore we only compared the displacement derivative within the calibrated area for shearography and FEM. The coordinate origin is at point O as shown in Fig. 5(b), which is the central point of D60-Z15. For determining the accuracy of the thick composite model, the displacement gradients along axis a-a are compared for simulations and experiments, as shown in Fig. 7(g), the difference of surface strain component along axis a-a by shearography and by modelling is shown in 7(h). The modelling results agree well with the shearography results within the range from −30 mm to 130 mm (with a maximum difference of $20\mu\varepsilon$). The difference between shearography and FEM increases out of this range, mainly because it is difficult to achieve a uniform heating over the whole surface of the specimen. In a real experiment, the heat flux to the edge region can be smaller than the estimated value.

Fig. 8 shows the out-of-plane displacement derivative maps at two cooling times by FEM and shearography. The reference speckle images were captured right after heating and the signal speckle images were

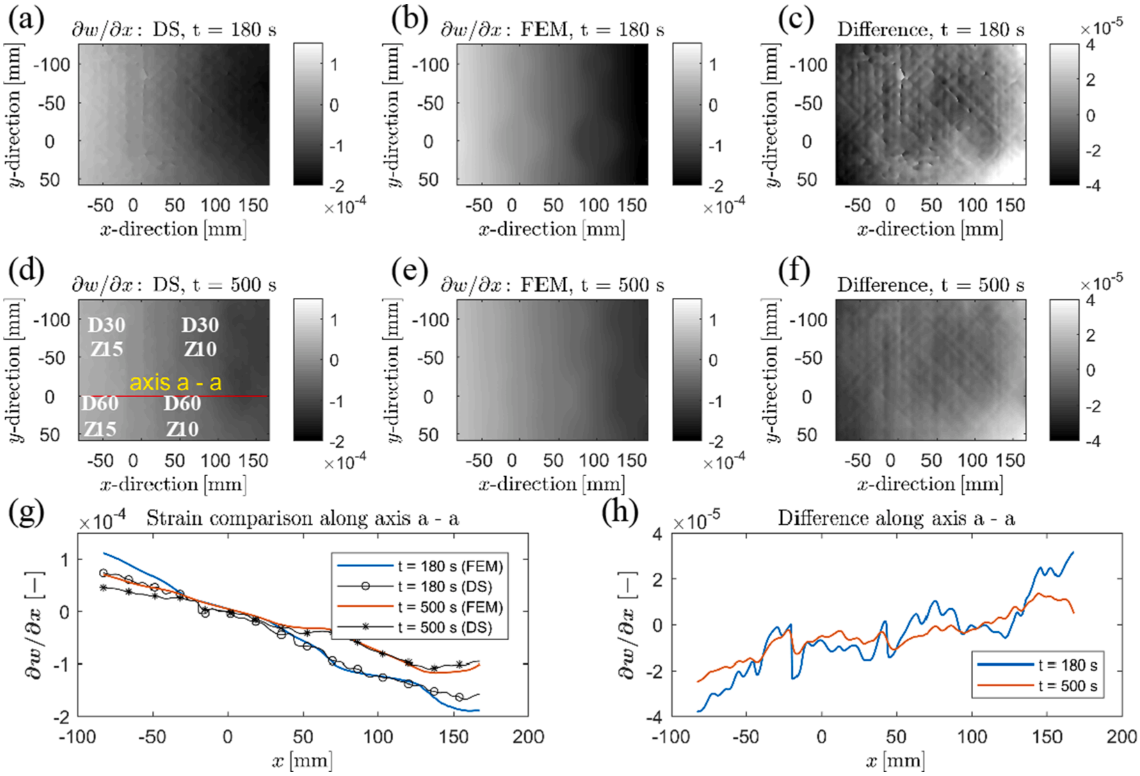

Fig. 7. Comparison of surface strain components (∂*w*/∂*x*) by shearography and by FEM at 180 s and 500 s (reference status: before heating). (a) - (c) Shearography result, FEM prediction, and corresponding difference at 180 s. (d) - (f) Shearography result, FEM prediction, and corresponding difference at 500 s. (g) Strain comparison along axis a - a for the simulations and experiments. (h) Difference in strain along axis a – a for the simulations and experiments.

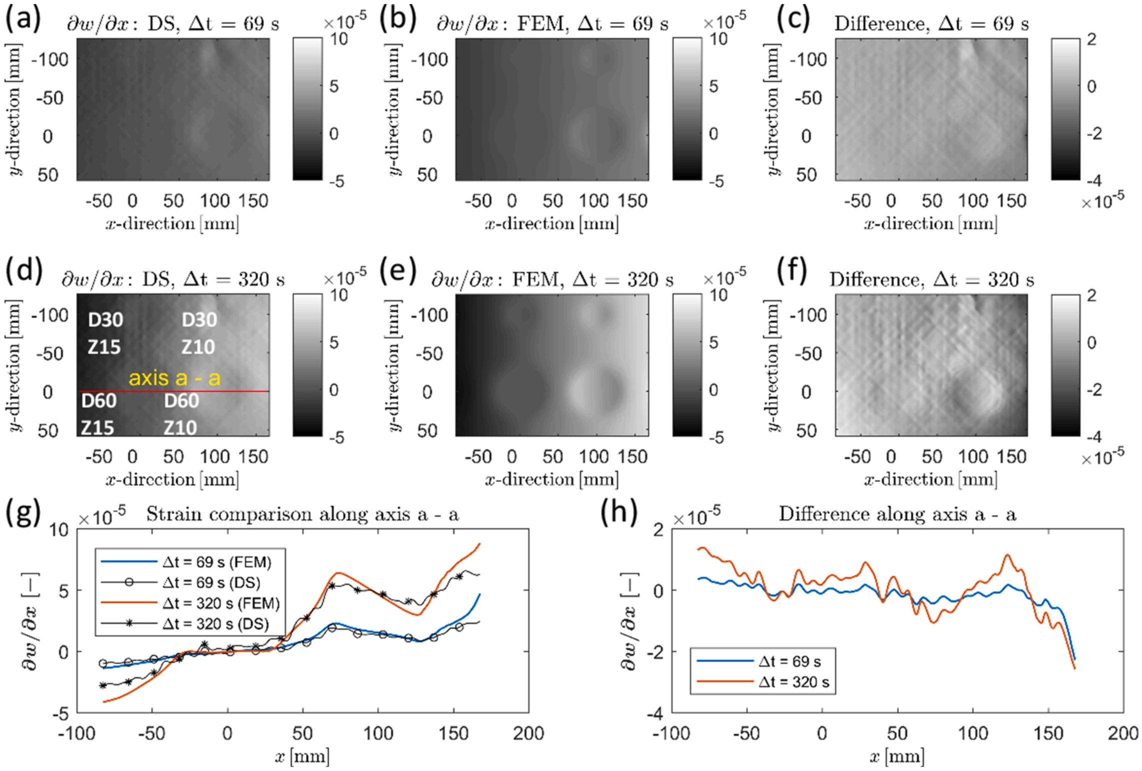

Fig. 8. Comparison of surface strain components (∂*w*/∂*x*) at two cooling time by shearography and by FEM (reference status: after heating): (a) - (c) Shearography result, FEM prediction, and corresponding difference after 69 s cooling. (d) - (f) Shearography result, FEM prediction, and corresponding difference after 320 s cooling. (g) Strain comparison along axis a - a for the simulations and experiments. (h) Difference in strain along axis a – a for the simulations and experiments.

captured after 69 s and 320 s cooling, respectively. The cooling times were chosen from when defects become visually detectable. As in Fig. 8 (a) and 8(b), after 69 s cooling, two circular regions along axis x = 100 mm are shown, representing defects D30-Z10 and D60-Z10 at 10 mm depth. After 320 s cooling, two more defects (D30-Z15 and D60-Z15) at 15 mm depth are visible in Fig. 8(d) and (e). The displacement derivative maps shown in Fig. 8 represent overall deformation of the specimen, which contains defect-induced deformation.

Fig. 8(g) shows the comparison of the displacement derivative along axis a-a between experiments and simulations at the two cooling times. In general, the displacement derivative increases from $x = -50$ mm to $x = 150$ mm, and a fluctuation in displacement derivative happens when encountering a defect. In FEM, the fiber and the resin were homogenised per layer, and therefore the simulated thermal deformation (lines in blue and orange in Fig. 8(g)) is smooth. While in experiments, it is shown that the displacement derivative curves measured with shearography (lines in black in Fig. 8(g)) are with local variations. The variations are mainly due to the local fiber deformation, which can be considered as a background noise.

Fig. 8(h) shows the difference in the displacement derivative between experiments and simulations at two cooling times, the difference after 69 s cooling shown as the blue line, and the difference after 320 s shown as the orange line. There is a significant variation at some points (e.g. at the hole edge of D60-Z10). This is mainly due to the fiber-deformation related noise. As the simulated thermal deformation is ideal while the experimental result is with local variations, therefore the difference between FEM and experiment as shown in Fig. 8(h) has variations from position to position. Besides, the manufacturing error when drilling holes in the thick composite can also contribute to the significant variations in Fig. 8(h). It can be noted that the actual depth of the artificial defects (D60-Z10 and D60–Z15) is larger than design values. Local variations in depth up to 1.5 mm were found which are not directly modelled. Therefore the defect signal measured by experiment is expected to be smaller than that predicted by FEM. Moreover, the mismatch in temperature between experiments and simulations can also be an issue. This mismatch is from the unknown heat transfer coefficient in experiments and the overestimated heat flux in FEM for the region far from the D60-Z15. The temperature difference between experiments and simulations increases with the cooling time (Fig. 6(c) and (d)), which may explain why the difference in displacement derivative between experiment and FEM increases as cooling time increases from 69 s to 320 s (Fig. 8(g) and (h)).

Defects are more visible in Fig. 8 than in Fig. 7, which indicates that using a reference state after heating has a better performance in defect detection compared with a reference state before heating. This is because the background signal (overall deformation) in Fig. 8 (10^{-5}) is much less than that in Fig. 7 (10^{-4}). Therefore, in the following sections, reference states after heating are used for shearography NDT.

4.2. Defect-induced deformation

Fig. 9 shows the process of deriving DID from OD. We first created a fitting surface based on the original displacement derivative map. The subtraction between the displacement derivative map and the fitting surface represents the DID. Fig. 10 shows the DID by experiment and by FEM, and the corresponding difference at two different cooling times (69 s and 320 s, respectively). The two cooling times are the same as in Fig. 8. The comparison of DID along axis a-a at two cooling times are shown in Fig. 10(g) and 10(h). Two fluctuations are clear to see at x = 0 mm and x = 100 mm for both the experimental and the FEM results in Fig. 10(h). These depict DID of defects D60 Z15 and D60-Z10, respectively. The difference between experiments and simulations along axis a-a is given in Fig. 10(i). The dotted line represents the difference between experiment and FEM after 69 s cooling, and the solid line represents the difference between experiment and FEM after 320 s cooling.

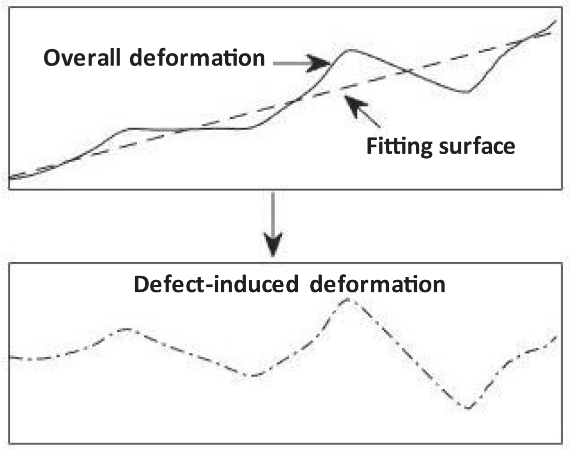

Fig. 9. Demonstration for deriving Defect-induced deformation from overall deformation (Gradient).

Lines at ±45° and 90° are clearly shown in Fig. 10(a) and (d) by experiment. Those lines represent fiber-related deformation, which are absent in Fig. 10(b) and (e) by FEM since the effect of composite material composition on strain was not considered separately. Similar to Fig. 8(g) and (h), there is a significant variation at some points the edge of the D60-Z10, and the difference in displacement derivative between experiment and FEM increases as cooling time increases from 69 s to 320 s (Fig. 10(g)–(i)). The possible reasons include the fiber-deformation related noise (~23% error in strain) in experiments, the local variations in defect depth (~19% error in strain) due to the manufacturing error, and the mismatch in temperature (~10% error in temperature) from the unknown heat transfer coefficient and the overestimated heat flux, which have been discussed in detail in Section 4.1. Besides, the fitting process (in Fig. 9) may also introduce extra error that contributes in the significant variations, which is difficult to assess accurately. However, it is expected to be a minor issue.

The simulated phase maps and the corresponding simulated strain maps by FEM are ideal without considering fiber-related noise and errors from the shearography system (error of speckle, error of phase, intensity error, etc.). Therefore, the background signal in the healthy region by FEM is much less than that by shearography. For our experiments, the standard deviation (STD) of the background phase signals in the healthy region by simulation and by experiment are approximately 0.02 rad and 0.2 rad, respectively. Practically in the shearography experiments, a phase measurement sensitivity of $\frac{2\pi}{10}$ rad [49] is possible to achieve, which is about three times of the STD of the background phase signals in healthy region in the experiment. Therefore in this paper, we set the thresholds for defect-induced phase (DIP) change $\delta\phi_{DIP}$ to be $\pm\frac{2\pi}{10}$ and $\pm\frac{2\pi}{5}$:

$\delta\phi_{DIP} \in \left[\infty, -\frac{2\pi}{5}\right] \cup \left[\frac{2\pi}{5}, \infty\right]$, the defect detection is most likely to succeed.

$\delta\phi_{DIP} \in \left(-\frac{2\pi}{5}, -\frac{2\pi}{10}\right) \cup \left(\frac{2\pi}{10}, \frac{2\pi}{5}\right)$, the defect detection is possible to succeed.

$\delta\phi_{DIP} \in \left[-\frac{2\pi}{10}, \frac{2\pi}{10}\right]$, the defect detection most likely will not to succeed.

Combining with Eq. (3), we can therefore derive the corresponding thresholds for DID and estimate the required cooling time. In this paper, the laser wavelength is 532 nm (green), and the mean of the shear amount δx over the calibration area is about 5.58 mm, the corresponding thresholds for defect-induced deformation $\frac{\partial w}{\partial x_{DID}}$ are ±4.8 and $\pm 9.5\mu\varepsilon$.

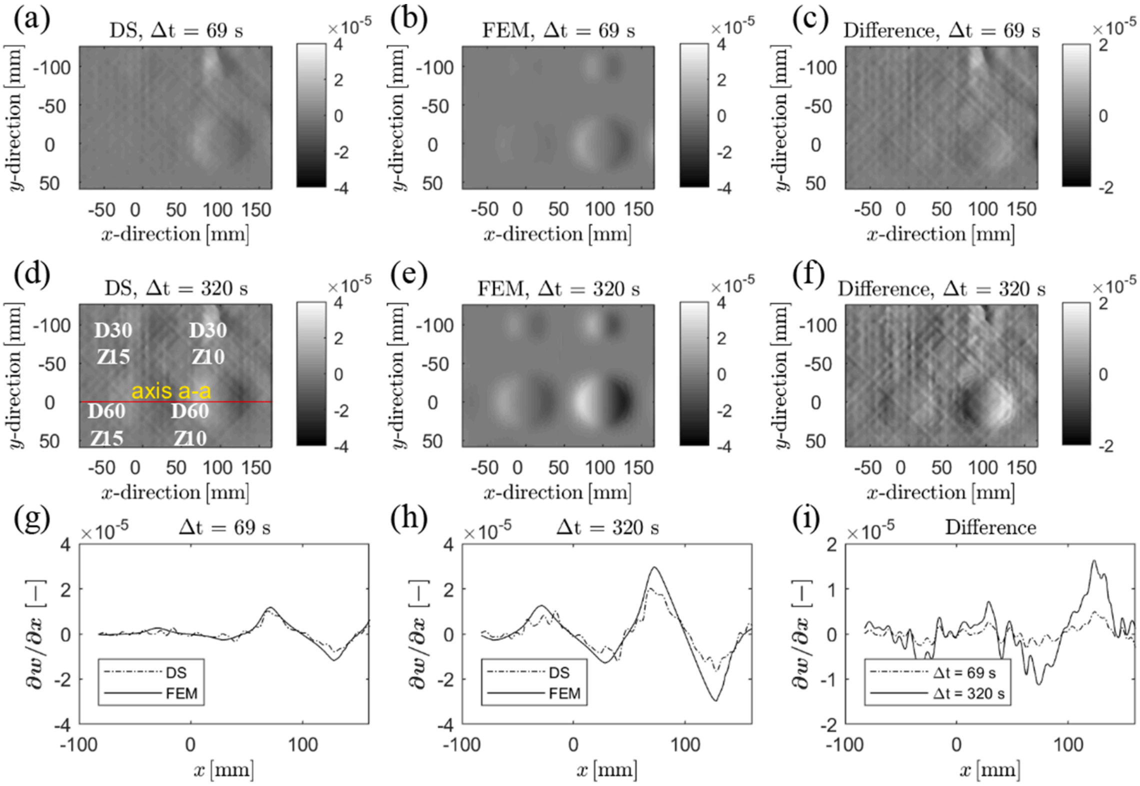

Fig. 10. Comparison of DID by experiment and by FEM at two cooling times: (a) - (c) Shearography result, FEM prediction, and corresponding difference after 69 s cooling. (d) - (f) Shearography result, FEM prediction, and corresponding difference after 320 s cooling. (g) – (i) DID comparison and corresponding difference along axis a - a for the simulations and experiments.

The DID during cooling along the axis a-a of the full model is shown in Fig. 11. For the heating scenario (heating from t = 0 to 180 s, cooling from t = 180 to 500 s) in this paper, the detectable depth is 15 mm, and the estimated cooling time for detecting the defect at 15 mm depth is around 250 s. Deeper defects may require more heating flux and/or more cooling time to be detectable. The follow–up experimental results show that the defect at 20 mm depth (D60-Z20) can be detected successfully with a heat flux of more than $1000W/m^2$. However, the detection of defects at 40 mm depth has not succeeded yet after testing various combinations of heat fluxes and heating times.

4.3. Effect of mechanical boundary conditions

Although it is possible to study the effects of mechanical boundary condition using experiments, for the GFRP panel under investigated in this paper, an ideal mechanical boundary condition (physically in the laboratory) such as fully clamped (CCCC) or simply supported-horizontal (UZ = 0) would be difficult to achieve. This is because of the relatively large size (600 × 450 mm^2) and the significant thickness (~50 mm). Therefore an experimental study of the effects of mechanical boundary conditions for this GFRP panel is challenging. With the numerical and experimental results reported in Sections 4.1 and 4.2, it is safe to say that the FEM model is reliable (maximum strain difference between simulations and experiments over the calibrated area during cooling is around $20\mu\varepsilon$). Since the simulations showed reasonable accuracy compared with shearography experiments, it was possible to study the effect of mechanical boundary conditions on DID by FEM. For this purpose, three mechanical boundary conditions are studied in this

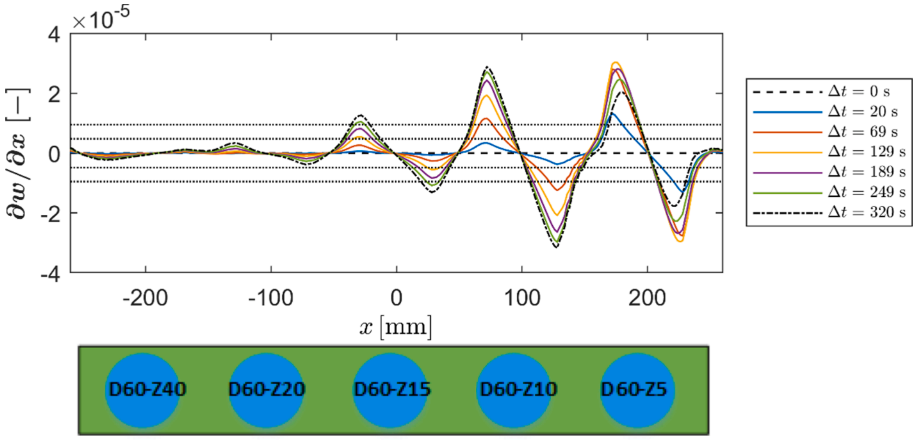

Fig. 11. DID along axis a-a during cooling by FEM, the thresholds for DID marked in dotted lines.

section, which are the freestanding case (UY = 0 for bottom surface, previously studied in 4.1), fully clamped case (CCCC), and the simply supported-horizontal case (UZ = 0 for back surface), as shown in Fig. 12. The specimen is heated and inspected from the front surface, which is the defect-free side. The constant surface heat flux, the heating and cooling times are set the same as in Section 4.1. The heat loss from the composite to environment is also the same as in Section 4.1. Hence, the temperature distributions in the composite for all three cases are the same, and the mechanical boundary condition is the only variable.

Fig. 13 shows the comparison of the three mechanical boundary conditions on DID after cooling for 320 s. The reference images were captured after 180 s heating. As shown in Fig. 13(a)–(c), shearographic fringes were simulated for a direct comparison of the three boundary conditions with the same shear distance of 5.58 mm. It can be noted that the simulated fringes highly depend on boundary conditions. For the freestanding case, the influence of whole body bending on the fringes is dominant, while for the fully clamped case and the simply supported-horizontal case, the magnitude of the body bending is much smaller compared with the freestanding case. Therefore, the defect-induced anomalies are more visible from the fringe patterns for the fully clamped case and the simply supported-horizontal case than for the freestanding case. The DID for the three boundary conditions is shown in Fig. 13(d) – 12(f) and the comparison along axis a-a is given in Fig. 13 (g). It shows that during cooling, the effect of boundary conditions on the DID at a large depth (more than 10 mm) is limited. The relative DID values of the three boundary conditions are close to each other. While for defects at 5 and 10 mm depth, there is a relatively big difference in DID among the three boundary conditions, which could be the effect of local stiffness.

Fig. 14 shows the DID of defects with the diameter of 60 mm at 5, 10, 15, 20 mm depth for three boundary conditions during cooling, the selected points are around the edge of the defect. When the depth of the defect is increased from 5 to 20 mm, the difference in the defect-induced strain among the three boundary conditions decreases from 11.9 to 1.7 $\mu\varepsilon$, which indicates that as defect depth increases, the influence of mechanical boundary conditions on DID decreases.

5. Conclusions

A numerical-experimental study has been conducted to investigate the defect detection capabilities of shearography NDT for a 51 mm thick GFRP laminate with flat bottom holes. First a thermal–mechanical model for detecting defects in the thick composite was developed. The model was then evaluated by TCs and shearography tests. It shows a good agreement in transient temperature and in strain maps between simulations and experiments. Based on the FEM and experimental results, the detectable depth of shearography for this thick GFRP laminate can be up to 20 mm with the current heating sources. It can be noted that the maximum detectable depth of shearography in fiber-reinforced composite laminates that can be found in literature is less than 10 mm [1,23,50]. Moreover, to the best of our knowledge, the defect detection capability of shearography in thick fiber reinforced composite laminates (with the thickness of more than 50 mm) has not reported yet. The thresholds for DIP and the corresponding DID are also determined for shearography testing in this paper. Besides, the effect of mechanical boundary conditions on DID was studied by FEM. It shows that mechanical boundary conditions have a significant influence on shearography fringe pattern. As for DID during cooling, the influence of boundary conditions for deep defects is limited, which may indicate that for thick composite inspection, the influence of mechanical boundary conditions on defect detection capabilities of shearography is limited in the case that the overall deformation can be removed properly.

The novelty of this study is that developing a suitable and sophisticated NDT method for thick composite is an urgent challenge to improve the safety, reliability and maintenance of these structures. In spite of the significance of thick composite inspection, few studies are available on this subject because of the complexity in material structures, the significant thickness, and the high stiffness of the thick composites. So far, the NDT defect detection capabilities and inspection limitations for thick composite have not been fully characterised. The experimental research for thick composite inspection with shearography was conducted by few researchers. No literature has reported on a numerical and experimental study on the defect detection capability of shearography in thick fiber reinforced composite laminates with the thickness of more than 50 mm, which is the main objective of this investigation. Besides, the investigation of DID to different loading conditions including loading time and loading intensity for thick composite inspection with shearography has not been reported, and there is little research about the effect of boundary conditions on DID of thick composite. From the above numerical and experimental investigation, it is clear that shearography is a promising NDT method for thick composite inspection. The presented numerical-experimental analysis and conclusions can provide valuable instruction on shearography NDT of thick composites. The established thermal–mechanical model can be used to assist in the shearography inspection by determining a reasonable loading intensity and loading time for inspection with shearography.

We aim at broadening of this shearography application to composites with thickness as up to 50–60 mm, also to bring the technique out of the laboratory in the nearest future. Future works include optimization of loading parameters to improve defect detection of shearography in thick composites and exploring the possibilities of both in-plane and out-of-plane deformation for other defects such as fiber breakage. Besides,

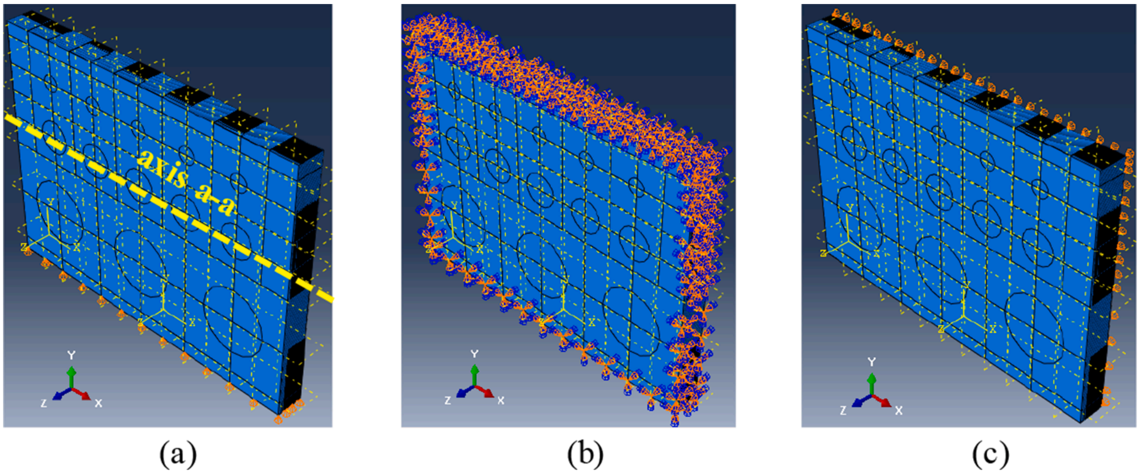

Fig. 12. Three mechanical boundary conditions for modelling. (a) Freestanding (UY = 0). (b) Fully clamped (CCCC). (c) Simply supported-horizontal (UZ = 0).

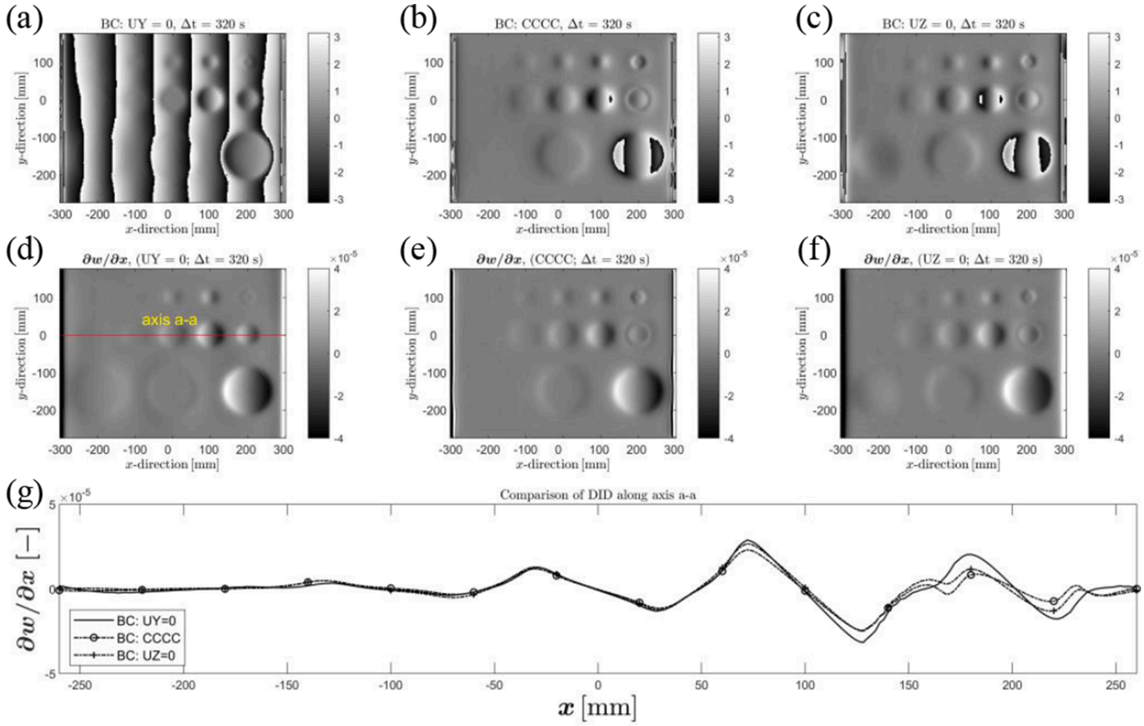

Fig. 13. Comparison of boundary conditions on DID after 320 s cooling by FEM (unit: [-]). (a) - (c) Simulated fringes for freestanding (UY = 0), full-clamped (CCCC), and simply supported-horizontal (UZ = 0), respectively. (d) - (f) DID for freestanding (UY = 0), full-clamped (CCCC), and simply supported–horizontal (UZ = 0), respectively. (g) Comparison of DID along axis a-a.

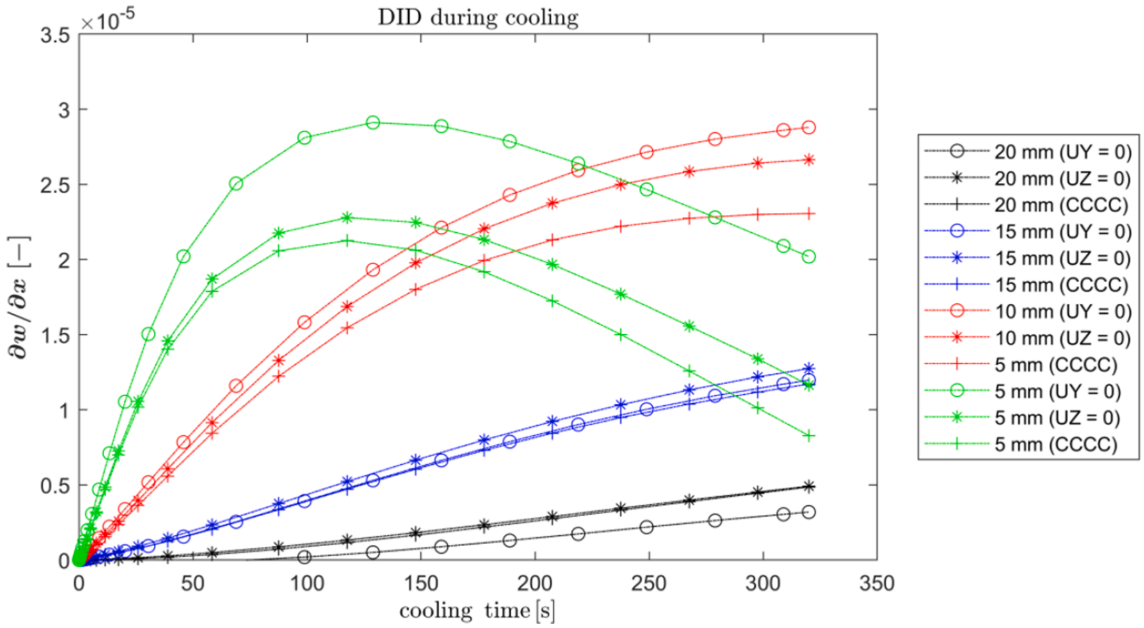

Fig. 14. DID of defects with the diameter of 60 mm at 5, 10, 15, 20 mm depth during cooling by FEM.

more boundary conditions (e.g. simply supported and cantilever) will be considered. Some suggestions for conducting experimental tests can be making the size of the specimen not too big (e.g. less than 300 × 300 mm^2), otherwise it may make the clamping much more difficult. Besides, more attention should be paid when selecting a suitable material for a clamping frame. Titanium may be suggested considering its high stiffness and low thermal expansion coefficient.

CRediT authorship contribution statement

Nan Tao: Methodology, Formal analysis, Software, Investigation, Writing – original draft, Visualization. **Andrei G. Anisimov:** Conceptualization, Software, Supervision, Writing – review & editing, Visualization. **Roger M. Groves:** Supervision, Writing – review & editing, Project administration, Funding acquisition.

Declaration of Competing Interest

The authors declare that they have no known competing financial interests or personal relationships that could have appeared to influence the work reported in this paper.

Acknowledgment

We would like to thank Damen Shipyards Group and namely Marcel Elenbaas and Athanasios Droutsas for the materials and the industrial feedback, and Marlies Nijemeisland from DASML for her contribution in performing the TMA and MDSC tests, and Durga Mainali from DASML for his contribution in performing the density and fiber volume ratio tests. This research was supported by the Operationeel Programma Zuid-Nederland (Op-Zuid) Project as part of the Dutch Composite Maintenance Centre (DCMC), supported by the Europees Fonds voor Regionale Ontwikkeling (EFRO) and the North Brabant province of the Netherlands.

Appendix A. Supplementary material

Supplementary data to this article can be found online at https://doi.org/10.1016/j.compstruct.2021.115008.

References

[1] Greene E. Inspection techniques for marine composite construction and NDE. Rep No SSC-463, United States Sh Struct Committee, Washington, DC; 2012.

[2] Mouritz AP, Gellert E, Burchill P, Challis K. Review of advanced composite structures for naval ships and submarines. Compos Struct 2001;53(1):21–42.

[3] Groves RM. 3.12 Inspection and Monitoring of Composite Aircraft Structures. In: Beaumont PWR, Zweben CH, editors. Compr. Compos. Mater. II, Oxford: Elsevier; 2018, p. 300–11.

[4] Montanini R, Freni F. Non-destructive evaluation of thick glass fiber-reinforced composites by means of optically excited lock-in thermography. Compos Part A Appl Sci Manuf 2012;43(11):2075–82.

[5] Ibrahim ME. Nondestructive evaluation of thick-section composites and sandwich structures: a review. Compos Part A Appl Sci Manuf 2014;64:36–48.

[6] Liu Z, Gao J, Xie H, Wallace P. NDT capability of digital shearography for different materials. Opt Lasers Eng 2011;49(12):1462–9.

[7] Nsengiyumva W, Zhong S, Lin J, Zhang Q, Zhong J, Huang Y. Advances, limitations and prospects of nondestructive testing and evaluation of thick composites and sandwich structures: a state-of-the-art review. Compos Struct 2021;256:112951. https://doi.org/10.1016/j.compstruct.2020.112951.

[8] Revel GM, Pandarese G, Cavuto A. Advanced ultrasonic non-destructive testing for damage detection on thick and curved composite elements for constructions. J Sandw Struct Mater 2013;15(1):5–24.

[9] Das P, Muni MK, Sahu SK. On crack detection in a laminated glass/epoxy composite beam under free vibration with fuzzy logic aid. Int J Struct Stab Dyn 2021:2150176.

[10] Sinha L, Das D, Nayak AN, Sahu SK. Experimental and numerical study on free vibration characteristics of laminated composite plate with/without cut-out. Compos Struct 2021;256:113051. https://doi.org/10.1016/j.compstruct.2020.113051.

[11] Sahu SK, Das P. Experimental and numerical studies on vibration of laminated composite beam with transverse multiple cracks. Mech Syst Signal Process 2020; 135:106398. https://doi.org/10.1016/j.ymssp.2019.106398.

[12] Panda HS, Sahu SK, Parhi PK, Asha AV. Vibration of woven fiber composite doubly curved panels with strip delamination in thermal field. J Vib Control 2015;21(15): 3072–89.

[13] Panda HS, Sahu SK, Parhi PK. Effects of moisture on the frequencies of vibration of woven fibre composite doubly curved panels with strip delaminations. Thin-Walled Struct 2014;78:79–86.

[14] Hung YY. Shearography for non-destructive evaluation of composite structures. Opt Lasers Eng 1996;24(2-3):161–82.

[15] Yang L, Li J. Shearography. In: Ida N, Meyendorf N, editors. Handb. Adv. Non-Destructive Eval., Cham: Springer International Publishing; 2018, p. 1–37.

[16] Hung YY. Applications of digital shearography for testing of composite structures. Compos Part B Eng 1999;30(7):765–73.

[17] Zhu Y, Tian G, Lu R, Zhang H, Engineering O. A review of optical NDT technologies 2011:7773–98.

[18] Steinchen W, Yang L, Kupfer G, Mäckel P. Non-destructive testing of aerospace composite materials using digital shearography. Proc Inst Mech Eng Part G J Aerosp Eng 1998;212(1):21–30.

[19] Zhao Q, Dan X, Sun F, Wang Y, Wu S, Yang L. Digital shearography for NDT: phase measurement technique and recent developments. Appl Sci 2018;8.

[20] Francis D, Tatam RP, Groves RM. Shearography technology and applications: a review. Meas Sci Technol 2010;21(10):102001. https://doi.org/10.1088/0957-0233/21/10/102001.

[21] Newman JW. 7.13 Shearography Nondestructive Testing of Composites. In: Beaumont PWR, Zweben CH, editors. Compr. Compos. Mater. II, Oxford: Elsevier; 2018, p. 270–90.

[22] Krutul EC, Groves RM. Opto-mechanical modelling and experimental approach to the measurement of aerospace materials using shearography and thermal loading. In: Bodermann B, editor. Model. Asp. Opt. Metrol. III, vol. 8083, SPIE; 2011, p. 434–42.

[23] De Angelis G, Meo M, Almond DP, Pickering SG, Angioni SL. A new technique to detect defect size and depth in composite structures using digital shearography and unconstrained optimization. NDT E Int 2012;45(1):91–6.

[24] Vandenrijt J-F, Xiong H, Lequesne C, Blain P, Georges M. Shearography inspection of monolithic CFRP composites: finite element modeling approach for assessing an adequate strategy of artificial defects representing delamination. In: Lehmann P, Osten W, Jr. AAG, editors. Opt. Meas. Syst. Ind. Insp. XI, vol. 11056, SPIE; 2019, p. 107–13.

[25] Akbari D, Soltani N, Farahani M. Numerical and experimental investigation of defect detection in polymer materials by means of digital shearography with thermal loading. Proc Inst Mech Eng Part B J Eng Manuf 2013;227(3):430–42.

[26] Yang Fu, Ye X, Qiu Z, Zhang B, Zhong P, Liang Z, et al. The effect of loading methods and parameters on defect detection in digital shearography. Results Phys 2017;7:3744–55.

[27] Buchta D, Heinemann C, Pedrini G, Krekel C, Osten W. Combination of FEM simulations and shearography for defect detection on artwork. Strain 2018;54(3): e12269. https://doi.org/10.1111/str.v54.310.1111/str.12269.

[28] Murri WJ, Sermon BW, Andersen RN, Martinez LA, der Heiden EJ, Garner CA. Defects in thick composites and some methods to locate them. In: Thompson DO, Chimenti DE, editors. Rev. Prog. Quant. Nondestruct. Eval. Vol. 10B, Boston, MA: Springer US; 1991, p. 1583–90.

[29] di Scalea FL, Spicer JB, Green RE. Electronic shearography with thermal loading for detecting debonds in thick polyurethane/ steel panels for marine applications. Res Nondestruct Eval 2000;12(1):43–51.

[30] Ibrahim ME. 7 - Nondestructive testing and structural health monitoring of marine composite structures. In: Graham-Jones J, Summerscales J, editors. Mar. Appl. Adv. Fibre-Reinforced Compos., Woodhead Publishing; 2016, p. 147–83.

[31] Summerscales J. 1 - Materials selection for marine composites. In: Pemberton R, Summerscales J, Graham-Jones J, editors. Mar. Compos., Woodhead Publishing; 2019, p. 3–30.

[32] Tran P, Ghazlan A, Nguyen TP, Gravina R. 3 - Experimental and theoretical damage assessment in advanced marine composites. In: Pemberton R, Summerscales J, Graham-Jones J, editors. Mar. Compos., Woodhead Publishing; 2019, p. 55–84.

[33] Standard A. D3039/D3039M-14. Stand Test Method Tensile Prop Polym Matrix Compos Mater; 2014.

[34] Standard A. DD3410/D410M-03. Stand Test Method Compressive Prop Polym Matrix Compos Mater with Unsupported Gage Sect by Shear Loading“, ASTM Int West Conshohocken, PA; 2003.

[35] Standard A. D7078/D7078M-12. Stand Test Method Tensile Prop Polym Matrix Compos Mater; 2012.

[36] Daniel IM, Ishai O. Engineering mechanics of composite materials. Oxford University Press; 2007.

[37] Shi L. Heat transfer in the thick thermoset composites; 2016.

[38] Rolfes R, Hammerschmidt U. Transverse thermal conductivity of CFRP laminates: a numerical and experimental validation of approximation formulae. Compos Sci Technol 1995;54:45–54.

[39] Zhu Y-K, Tian G-Y, Lu R-S, Zhang H. A review of optical NDT technologies. Sensors 2011;11(8):7773–98.

[40] Enie RB, Rizzo RR. Three-dimensional laminate moduli. J Compos Mater 1970;4 (1):150–4.

[41] Pagano NJ. Exact Moduli of Anisotropic Laminates. In: Reddy JN, editor. Mech. Compos. Mater. Sel. Work. Nicholas J. Pagano, Dordrecht: Springer Netherlands; 1994, p. 210–31.

[42] Chan WS, Lin CY, Liang YC, Hwu C. Equivalent thermal expansion coefficients of lumped layer in laminated composites. Compos Sci Technol 2006;66(14):2402–8.

[43] Sun CT, Li S. Three-dimensional effective elastic constants for thick laminates. J Compos Mater 1988;22(7):629–39.

[44] Hoorn N van, Kassapoglou C, Brink WM van den. Impact response prediction and sensitivity analysis of thick laminated composite plates; 2020.

[45] Kulkarni MR, Brady RP. A model of global thermal conductivity in laminated carbon/carbon composites. Compos Sci Technol 1997;57(3):277–85.

[46] Bergman TL, Lavine AS, Incropera FP, DeWitt DP. Fundamentals of heat and mass transfer. Wiley; 2017.

[47] Goto DT, Groves RM. Error analysis of 3D shearography using finite-element modelling. In: Gorecki C, Asundi AK, Osten W, editors. Opt. Micro- Nanometrology III, vol. 7718, SPIE; 2010, p. 281–92.

[48] Anisimov AG, Serikova MG, Groves RM. 3D shape shearography technique for surface strain measurement of free-form objects. Appl Opt 2019;58(3):498. https://doi.org/10.1364/AO.58.000498.

[49] Yang L, Xie X. Digital shearography: new developments and applications. SPIE 2016.

[50] Shang HM, Chau FS, Tay CJ, Toh SL. Estimating the depth and width of arbitrarily-oriented disbonds in laminates using shearography. J Nondestruct Eval 1990;9(1): 19–26.